Compression of matter by hyperspherical shock waves

2012 EPL 100 24004

(http://iopscience.iop.org/0295-5075/100/2/24004)

A Letters Journal Exploring the Frontiers of Physics

October 2012

EPL, **100** (2012) 24004
doi: 10.1209/0295-5075/100/24004

www.epljournal.org

Compression of matter by hyperspherical shock waves

M. Murakami[1], J. Sanz[1,2] and Y. Iwamoto[3]

[1] *Institute of Laser Engineering, Osaka University - 2-6 Yamada-oka, Suita, Osaka 565-0871, Japan*
[2] *ETSI Aeronauticos, Universidad Politecnica de Madrid - 3 Pza Cardenal Cisneros, Madrid 28040, Spain, EU*
[3] *Engineering Department, Graduate School of Ehime University - 3 Bunkyocho, Ehime 790-8577, Japan*

received 25 August 2012; accepted in final form 1 October 2012
published online 31 October 2012

PACS 47.40.Ki – Supersonic and hypersonic flows
PACS 52.35.Tc – Shock waves and discontinuities

Abstract – A novel compression scheme is proposed, in which hollow targets with specifically curved structures initially filled with uniform matter, are driven by converging shock waves. The self-similar dynamics is analyzed for converging and diverging shock waves. The shock-compressed densities and pressures are much higher than those achieved using spherical shocks due to the geometric accumulation. Dynamic behavior is demonstrated using two-dimensional hydrodynamic simulations. The linear stability analysis for the spherical geometry reveals a new dispersion relation with cut-off mode numbers as a function of the specific heat ratio, above which eigenmode perturbations are smeared out in the converging phase.

Introduction. – The shock wave is a most basic and important hydrodynamic phenomenon in many different branches of high-energy density physics. In converging geometries such as cylinders and spheres, a shock wave is cumulatively strengthened towards the center and exhibits asymptotically self-similar behavior. The self-similar solution of a spherical converging shock wave was first reported by Guderley [1] (also independently by Landau [2] and Stanukovich [3]). The work was followed by a number of subsequent investigations. For instance, Meyer-ter-Vehn and Schalk [4] gave comprehensive descriptions on the self-similar nature of cumulative shock waves together with important examples. There are also pioneering experimental works on cumulative shock waves with different geometries [5–7]. The significance of Guderley's work is not only that it solved the particular problem, but that it opened a view to a much broader class of self-similar solutions in gas dynamics. Moreover, it first shed light on the singular behavior of spherically imploding waves near the center.

The concept of spherical implosion has been extended to an important and practical application, inertial confinement fusion (ICF) [8], in which a small target sphere composed of deuterium-tritium (DT) fuel undergoes very high compression (thousands times the solid density) and high temperature ($\gtrsim 5\,\mathrm{keV}$) while being irradiated and driven by intense laser light. In particular, novel ICF ignition schemes such as impact ignition [9,10] and shock ignition [11] take advantage of the compression performance achieved with a strong converging shock. Note that an isentropic compression [12], which strongly contrasts with the shock compression, is regarded as an ideal approach to achieve very high material densities, especially for equation-of-state (EOS) studies as well as ICF, because the entropy increase and thus the required energy investment can be suppressed at the lowest level. In a typical ICF implosion, the isentropic compression and shock compression are best mixed along the temporal evolution of a fuel element to attain higher stability and energy coupling efficiency.

The self-amplifying nature of cumulative shocks is due to the area contraction of the shock surface, as described in the divergence operator, $r^{1-\nu}(\partial/\partial r)r^{\nu-1}$, of the mass conservation law, where r is the one-dimensional coordinate of the system and ν is the geometrical index, *i.e.*, $\nu = 1$, 2, and 3 represent plane, cylindrical, and spherical geometries, respectively. The degree of shock-compressed densities and pressures increases with the geometrical index ν. In most analytical and numerical studies, these integers have been employed for the geometrical index. It is then a straightforward conjecture that even higher compression performance by cumulative shocks could be achieved with a higher geometrical number $\nu > 3$, though creating such a super-geometrical structure is non-trivial.

Hyperspherical geometries. – Here we propose that arbitrary integers $\nu = 4, 5, \ldots$, or even non-integer or fractal numbers, can be considered as a practical system to achieve considerably higher shock compression than in

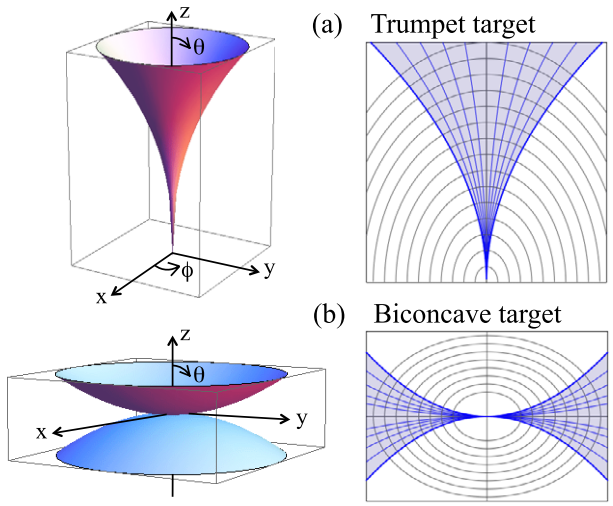

Fig. 1: Schematic views of two different types of hyperspherical geometry. The two configurations are symmetric with respect to the vertical z-axis. Uniform matter is filled in the blue-hatched volumes.

spherical geometry (below such compressions with $\nu > 3$ are referred to as hyperspherical compression). Figure 1 illustrates such configurations, where two different types of geometry, a) trumpet target and b) biconcave target, are given. Suppose that a uniform material is embedded in the hatched volume, which is encompassed by the curved wall to form a channel narrowing toward the center. The wall is assumed to be perfectly rigid in the present work. The embedded material has practically a limited mass and thus a boundary surface. A pressure pulse of some intermediate duration is then applied to the boundary surface. The compression wave is launched to develop into a strong converging shock that is transmitted toward the geometrical center. The converging shock is expected to transit to a self-similar regime as it approaches the center via the intermediate asymptotic regime [13].

Cartesian coordinates (x, y, z) inside those targets can be converted to more useful orthogonal curvilinear coordinates (r, θ, ϕ): $x^2 + y^2 = (\tan\theta)^2 z^{2\beta}$, $\beta(x^2 + y^2) + z^2 = r^2$, and $\tan\phi = y/x$, where all the parameters are dimensionless and $\beta = 1$ corresponds to the spherical geometry. The first and second relations describe the longitudinal and azimuthal curves, respectively, crossing each other at right angles. The hatched volumes in fig. 1 correspond to $0 \leqslant r$, $0 \leqslant \phi \leqslant 2\pi$, $0 \leqslant \theta \leqslant \theta_0$ $(\beta \geqslant 1)$, and $\frac{\pi}{2} - \theta_0 \leqslant \theta \leqslant \frac{\pi}{2} + \theta_0$ $(0 < \beta \leqslant 1)$, where θ_0 describes the inner wall of the casing. The constant β defines the shape of the ellipsoids and is related to the geometrical index ν, in the form, $\nu = 1 + 2\beta$ for $\beta \geqslant 1$ and $\nu = 2 + \beta^{-1}$ for $0 < \beta \leqslant 1$. We extend Guderley's analysis to address such hyperspherical shock compressions. The analytical prediction is supported by a two-dimensional hydrodynamic simulation, as shown later. For example, with $\nu = 6$ and a specific heat ratio $\gamma = 7/5$, a density compression rate as high as 265 times the initial density is demonstrated as a result of a single round-trip of strong shock waves, which is twice larger than that in the spherical geometry. Thus the present work suggests that strong shock compressions produced in some special geometries can provide a new approach to achieve extreme compressed states equally with isentropic compressions.

It is also important to examine the stability of a converging shock wave. It has been widely recognized that a spherically converging shock wave is always unstable [14,15]. We address a rigorous linear perturbation theory of spherical converging shock waves to show that a cut-off mode number exists, over which perturbations are diminished. This result is expected to give significant revision to our understanding on the nature of a spherically converging shock wave. The local open angle of the channel and thus a reciprocal of the corresponding spherical mode number progressively reduce toward the center. As a result, the fluid motion in such a narrowing channel becomes asymptotically pseudo one-dimensional [7] (depending only on r) close to the origin, which justifies the one-dimensional self-similar analysis given below.

Generalized Guderley's solution. – The one-dimensional hydrodynamic system is given by

$$\frac{\partial \rho}{\partial t} + \frac{1}{r^{\nu-1}} \frac{\partial}{\partial r} \left(r^{\nu-1} \rho v \right) = 0, \tag{1}$$

$$\left(\frac{\partial}{\partial t} + v \frac{\partial}{\partial r} \right) v = -\frac{1}{\rho} \frac{\partial p}{\partial r}, \tag{2}$$

$$\left(\frac{\partial}{\partial t} + v \frac{\partial}{\partial r} \right) \ln \frac{p}{\rho^\gamma} = 0, \tag{3}$$

where $\rho(r,t)$, $p(r,t)$, and $v(r,t)$ are the density, pressure, and the "radial" velocity, respectively, as functions of "radius" r and time t. In eq. (3), the adiabatic relation of an ideal gas is postulated. The origin for time $t = 0$ is taken to be at the instant of shock collapse. The shock front radius $R(t)$ is assumed to be given in the power law form, $R = A|t|^\alpha$, with an appropriate constant A and unknown dimensionless number α, which will only be determined numerically as an eigenvalue problem. The numerical treatment to determine the eigenvalue is given in appendix A, where the original Guderley's model for spherical geometry $(\nu = 3)$ is generalized to treat an arbitrary value of ν.

Figure 2 shows the numerical results for $\nu = 3$ (spherical) with $\gamma = 5/3$. Panel (a) plots trajectories of the shock front and a fluid element, where the time is normalized such that the fluid element is hit by the converging shock at $t/\tau = -1$ (where τ is a time constant). Both the shock speed and the fluid speed evolve over time, contrasting with the planar case where the speeds are kept constant. Panel (b) plots temporal evolutions of the normalized pressure p/p_1, and the density ρ/ρ_0 of the fluid element specified in panel (a), where p_1 denotes the pressure generated by the converging shock at $t/\tau = -1$. The shock-compressed fluid elements are further compressed adiabatically to keep their entropy constant during the

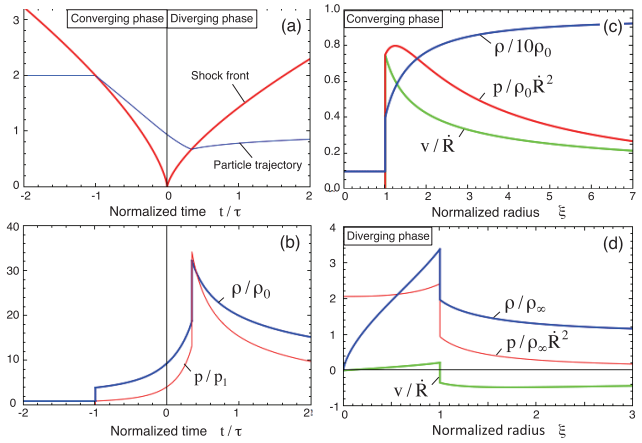

Fig. 2: Numerical results for the shock dynamics obtained from the self-similar solution with $\nu = 3$ (spherical) and $\gamma = 5/3$.

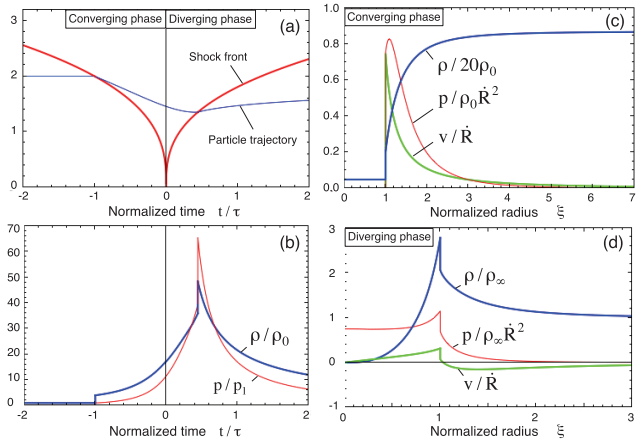

Fig. 3: Similar numerical results to those in fig. 2 but with $\nu = 9$ (hyperspherical) and $\gamma = 5/3$.

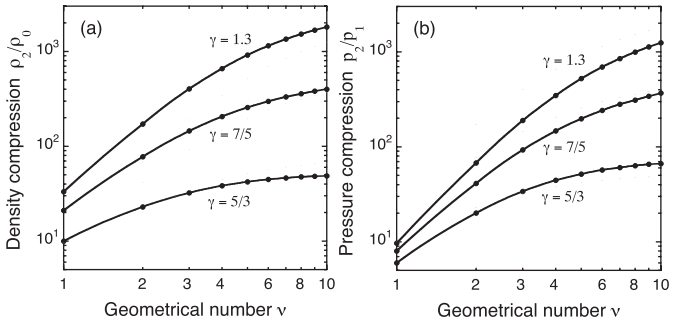

Fig. 4: Peak values for (a) normalized density ρ_2/ρ_0 and (b) pressure p_2/p_1 for a fixed fluid element, which are attained at the moment when a fluid element encounters the reflecting (2nd) shock. The suffixes, 0, 1, and 2, denote the initial, 1st-shocked, and 2nd-shocked states, respectively.

Table 1: Eigenvalues for hyper-shock compression; $\tilde{\rho_1} = \rho_\infty/\rho_0$, $\tilde{\rho_2} = \rho_2/\rho_0$, and $\tilde{p} = p_2/p_1$, where ρ_0, ρ_∞, and ρ_2 denote the initial density, the density at $\xi = \infty$, and the maximum density on the reflected shock surface, respectively, which are all constant in time; p_1 and p_2 are the pressures of a fixed fluid element at the first and second hit by shock, respectively.

	$\gamma = 5/3$				$\gamma = 7/5$			
ν	α	$\tilde{\rho_1}$	$\tilde{\rho_2}$	$\tilde{p}$	α	$\tilde{\rho_1}$	$\tilde{\rho_2}$	$\tilde{p}$
1	1	4	10	6	1	6	21	8
2	0.8156	7.02	23.0	20.1	0.8354	12.9	77.7	41.3
3	0.6884	9.55	32.3	34.0	0.7172	20.1	145	93.1
4	0.5954	11.6	38.4	44.5	0.6283	26.8	206	147
5	0.5245	13.2	42.2	51.6	0.5590	33.0	257	198
6	0.4687	14.6	44.8	57.2	0.5035	38.4	298	242
7	0.4236	15.7	46.4	60.6	0.4580	43.4	332	281
8	0.3865	16.6	47.6	63.4	0.4200	47.8	358	311
9	0.3553	17.4	48.3	65.5	0.3879	51.7	382	341
10	0.3288	18.1	48.7	66.7	0.3603	55.4	401	366

transition period until they encounter the reflected shock. After the reflected shock passes, the fluid elements expand at relatively slow speeds. Panel (c) depicts spatial profiles of the normalized pressure $p/\rho_0\dot{R}^2$, the density ρ/ρ_0, and the fluid velocity $v/\dot{R}$, in the converging phase, while Panel (d) shows spatial profiles in the diverging phase, $p/\rho_\infty\dot{R}^2$, ρ/ρ_∞, and $v/\dot{R}$, where $\rho_\infty = \rho_0 G_0(\infty)$ is the density at infinity. In panel (c), the density ultimately reaches $\rho_\infty/\rho_0 \simeq 9.55$ after the first shock compression, $\rho/\rho_0 = (\gamma+1)/(\gamma-1) = 4$, due to the adiabatic compression.

Figure 3 shows the corresponding results for the hyperspherical case with $\nu = 9$, which strongly contrasts with the spherical case given in fig. 2. The spatial structures of the quantities, p, ρ, and v, are formed in a narrower space than in fig. 2 after the passage of the converging and diverging shocks. The maxima of the compression rates for the density and pressure are respectively $\rho_2/\rho_0 \simeq 48.5$ and $p_2/p_1 \simeq 65.5$, which are achieved by a round-tripping shock wave at different times by different fluid elements, but are kept constant in time as a whole. These characteristic values are conspicuously higher than $\rho_2/\rho_0 \simeq 32.3$ and $p_2/p_1 \simeq 34.2$ in fig. 2. Figure 4 summarizes the compression performance of ρ_2/ρ_0 and p_2/p_1 for three different specific heat ratios, $\gamma = 5/3$, 7/5, and 1.3. It is apparent that a lower γ results in substantially higher compression performance, *e.g.*, $\rho_2/\rho_0 \simeq 400$ and $p_2/p_1 \simeq 365$ with $\gamma = 7/5$ (a diatomic gas) at $\nu = 10$, only by a single round-trip shock compression. Although we have assumed perfect adiabaticity, the practical value of γ that describes the thermodynamic relation $p \propto \rho^\gamma$ can be reduced by entropy emission via electron or radiation heat conduction [16]. Thus, the present system can be extended to a more complex hydrodynamic problem with heat conductions. Important eigenvalues for α, ρ_∞/ρ_0, ρ_2/ρ_0, and p_2/p_1 are summarized in table 1 as a function of ν and γ.

Stability of spherical converging shock. – Here we present a linear perturbation theory for a spherically converging shock and resultant new growth rates of non-uniformities of the shock surface, σ; details of the

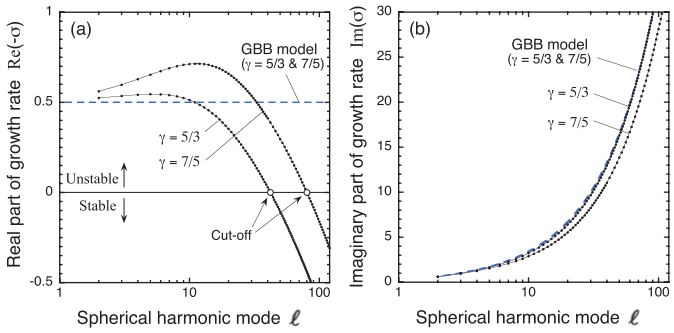

Fig. 5: Growth rates of perturbations in a spherical converging shock: (a) effective growth of amplitude, $\mathrm{Re}(-\sigma)$, and (b) oscillation frequency, $\mathrm{Im}(\sigma)$.

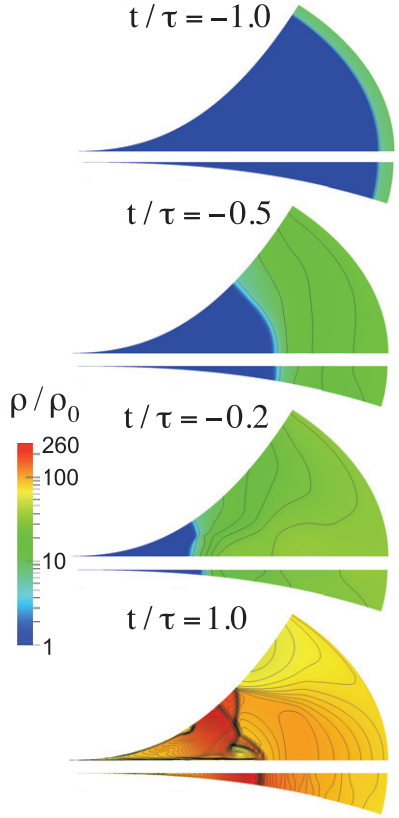

Fig. 6: Snapshots of a two-dimensiional simulation result at four sequential times for the density compression rate ρ/ρ_0 (only one-half pictures with respect to the symmetric axis) with $\nu = 6$ and $\gamma = 7/5$ fixed. The upper and lower figures at each time stand for wide- and narrow-angle trumpet targets, respectively, and are arranged closely for ease of comparison.

numerical treatment are given in appendix B. Thereby, the principle in finding σ is to solve the linearized system as an eigenvalue problem, so that the integrated curves for the perturbed quantities smoothly pass the sonic point $\xi = \xi_0$. Figures 5(a) and (b) show the numerical results thus obtained for the real part (effective growth of amplitude), $\mathrm{Re}(-\sigma)$, and the imaginary part (oscillation frequency), $\mathrm{Im}(\sigma)$, of the growth rate, respectively. The results obtained by Gardner, Book, and Bernstein [14] (labeled by "GBB") are also plotted for comparison. Despite the excellent agreement of the two models for $\mathrm{Im}(\sigma)$ in fig. 5(b), they exhibit strikingly different behavior for $\mathrm{Re}(-\sigma)$. The present theory reveals the existence of a cut-off mode number ℓ_c, over which perturbations diminish in the converging process, where $\ell_c \simeq 42$ for $\gamma = 5/3$ and $\ell_c \simeq 80$ for $\gamma = 7/5$. The physical explanation for the existence of the cut-off and stable region is given as follows. No information from the supersonic region ($\xi > \xi_0$) can reach the shock surface [17]. Therefore, the perturbation information can transmit reflectively and interact with each other in the subsonic region ($1 < \xi < \xi_0$). The wave superposition effect then acts to diminish the surface perturbation for wavelengths shorter than the distance between the shock surface and the sonic surface. This physical picture is similar to the thermal smoothing effect [18], and was not taken into account in the simplified GBB model based on the CCW (Chester-Chisnell-Whitham) theory [19–21], which only gives $\mathrm{Re}(-\sigma) = 1/2$ as an approximation valid for relatively low modes.

The above perturbation analysis for a fully spherical configuration can be directly applied to a cone target corresponding to $\nu = 3$ in fig. 1(a), with slight modifications: the polar component of the transverse velocity v_θ has to be null on the wall of the hollow solid-cone with a semi-apex angle, θ_0. This condition is formulated (for axisymmetric perturbations) by $v_\theta(\theta_0) \propto [\mathrm{d}P_\ell(\cos\theta)/\mathrm{d}\cos\theta]_{\theta=\theta_0} = 0$ (where P_ℓ is a Legendre polynomial), which restricts the possible set of ℓ and θ_0 such that $\ell \geqslant 1.22\pi/\theta_0$. The critical full apex angle Θ_c, that any eigenmode perturbation is expected to diminish for $\Theta < \Theta_c$, is given by $\Theta_c \approx 2.44\pi/\ell_c \sim 10^\circ$ for the cone target ($\gamma = 5/3$). The configuration shown in fig. 1(b) with $\nu = 3$ (*e.g.,* X-target [22]) is addressed in a similar manner: $\Theta_c (= \pi - 2\theta_0) \approx 1.88\pi/\ell_c$ for even-ℓ-modes ($\gamma = 5/3$). Note that, for this type of target, v_θ of all odd-ℓ-modes is null on the wall regardless of the θ_0-value, and therefore the dispersion relation $\sigma(\ell)$ is the same as in the full spherical case. Although the present perturbation theory applies only to spherical geometry ($\nu = 3$), it assists elucidation of the stability for $\nu > 3$; as the shock converges along $r \to 0$, the local open angle $\Theta(r)$ progressively decreases, and the converging shock is expected to be even more strongly stabilized as predicted above.

Two-dimensional hydrodynamic simulation. – Figure 6 shows snapshots of the flow in two different cone targets, in terms of ρ/ρ_0 obtained by two-dimensional hydrodynamic simulation with $\nu = 6$ and $\gamma = 7/5$. The upper and lower plots at each time correspond to a large and small open angles, respectively. The initial quasi–one-dimensional flow pattern is given by the self-similar solution. For the large-angle target, the jet grows on the shock front at $t/\tau = -0.2$, and in the diverging phase the shock waves and the wall multiply interact and

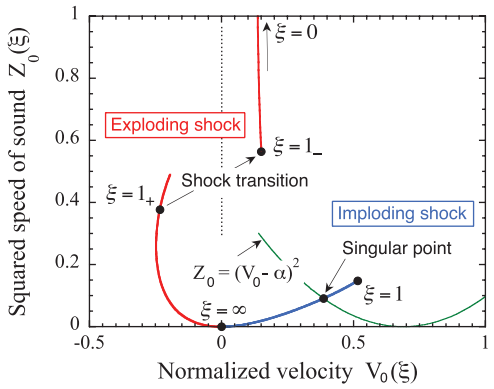

Fig. 7: (Colour on-line) An integrated curve on the (Z, V)-plane for $\nu = 3$ and $\gamma = 5/3$, which is drawn along $\xi = 1 \to \infty$ for the converging shock, while $\xi = \infty \to 1$ for the diverging shock.

lead to a turbulent mix state at $t/\tau = 1.0$. For the small-angle target, the entire process evolves in a quasi–one-dimensional manner, and no turbulent pattern is observed even at $t/\tau = 1.0$. This higher stability of the thinner cone target is explained by the linear perturbation theory. Furthermore, the maximum ρ_m and averaged densities of the shocked matter in fig. 6 are both close to those of the self-similar solution. For example, $\rho_m/\rho_0 \simeq 265$ is numerically observed at $t/\tau = 1.0$ for the large-angle target, which is already twice as large as that in the spherical case with $\rho_2/\rho_0 = 145$ (compare with table 1). Although we have assumed a perfectly rigid wall, any wall material will not withstand at extremely high pressures. A conceivable measure to suppress (or at least effectively delay) the wall collapse is to launch counter shock waves exerting symmetrically on the wall. This is likely to be realized, for instance, by sandwiching the hypershock target between similar structures, the shape of which will have to be carefully designed as well as the driving pulses.

Concluding remarks. – We have proposed novel structured targets, the shapes of which are characterized by the geometrical index ν, to achieve substantially higher shock-compressed densities and pressures than in spherical geometry. We have presented the self-similar solution for hyperspherical shock waves and the rigorous linear perturbation theory for a spherical converging shock. The geometrical cumulation effect has been clarified in terms of the density and pressure attainable by a single round-trip of a shock wave, *e.g.*, $\rho_2/\rho_0 \simeq 400$ and $p_2/p_1 \simeq 365$ with $\gamma = 7/5$ at $\nu = 10$. By controlling the practical value of γ via electron or radiation transport, the present scheme is expected to develop into more complex but attractive explorations. With respect to the stability, it has been revealed that a cut-off mode number dependent on γ exists, over which eigenmode perturbations diminish in the converging phase. This gives a prescription for practical designs of hyperspherical targets. The theoretical predictions given here have been confirmed by two-dimensional hydro-simulations. The present scheme has the potential to provide a new experimental tool for high compression of matter in different branches of high-energy density physics such as EOS studies under extreme conditions.

* * *

This work was supported by the Japan Society for the Promotion of Science (JSPS) and the Ministerio de Ciencia e Innovación of Spain (Grant No. ENE2010-19401; ENE2011-28489). One of the authors (JS) acknowledges the hospitality and support of the Institute of Laser Engineering.

Appendix A. – Following Guderley [1] and using the notations of ref. [17], the self-similar coordinate, $\xi = r/R = r/A|\,t\,|^{\alpha}$, and the self-similar fluid variables are introduced in the form

$$v = \frac{r}{t}V_0(\xi), \quad \rho = \rho_0 G_0(\xi), \quad \gamma\frac{p}{\rho} = \left(\frac{r}{t}\right)^2 Z_0(\xi), \quad \text{(A.1)}$$

where V_0, G_0, and Z_0, denote the dimensionless velocity, density, and squared speed of sound, respectively, with ρ_0 being the initial density. The original system, eqs. (1)–(3), is then reduced to the following system of ordinary differential equations (ODE):

$$\frac{\mathrm{d}V_0}{\mathrm{d}\ln\xi} = \frac{\nu Z_0(V_0-\mu) - V_0(V_0-1)\Phi_0}{\Delta_0}, \quad \text{(A.2)}$$

$$\frac{\mathrm{d}\ln G_0}{\mathrm{d}\ln\xi} = \frac{-1}{\Phi_0}\left(\nu V_0 + \frac{\mathrm{d}V_0}{\mathrm{d}\ln\xi}\right), \quad \text{(A.3)}$$

$$\frac{\mathrm{d}Z_0}{\mathrm{d}\ln\xi} = \left((\gamma-1)\frac{\mathrm{d}\ln G_0}{\mathrm{d}\ln\xi} - \frac{2(V_0-1)}{\Phi_0}\right) Z_0, \quad \text{(A.4)}$$

with $\mu = 2(1-\alpha)/\gamma\nu$, $\Phi_0 = V_0 - \alpha$ and $\Delta_0 = \Phi_0^2 - Z_0$. Along the so-called sonic line [2], $\Delta_0 = 0$, the fluid velocity relative to the line with $\xi = \xi_0$ becomes sonic, where ξ_0 is a specific constant of the system. Note that the adiabatic integral [17] of the present system is obtained from eqs. (A.3) and (A.4) in the form, $\xi^{2+\nu} Z_0 G_0^{2-\gamma} \Phi_0^{2(1-\alpha)/\nu\alpha} = c_0$, where c_0 is an integration constant.

To perform the numerical integration, the system is further simplified to a single ODE of $\mathrm{d}Z_0/\mathrm{d}V_0$, which is a function of only Z_0 and V_0. The entire system, eqs. (A.2)–(A.4), can thus be numerically integrated from $\xi = 1$ (shock surface) toward the infinity ($\xi = \infty$) in the converging phase, where the boundary conditions are given by

$$V_0(1) = \frac{2\,\alpha}{\gamma+1}, \quad G_0(1) = \frac{\gamma+1}{\gamma-1}, \quad Z_0(1) = \frac{\alpha\gamma V_0(1)}{G_0(1)}. \quad \text{(A.5)}$$

The condition under which the integral curve $Z_0(V_0)$ smoothly crosses the parabola $\Delta_0 = 0$ determines the similarity exponent α [2], and the curve then monotonically converges to the origin in the (V_0, Z_0)-plane, *i.e.*, $Z_0(\infty) = V_0(\infty) = 0$. In the diverging phase, after the converging

shock is reflected at the center ($\xi = 0$), the ODE system is integrated with the same eigenvalue of α but along the opposite direction, $\xi = \infty \to 0$.

Figure 7 shows the integrated curve on the (V_0, Z_0)-plane for spherical case ($\nu = 3$) with $\gamma = 5/3$ (*e.g.*, a monoatomic gas), which is drawn along $Z_0 \to 0$ in the converging phase, while $Z_0 \to \infty$ in the diverging phase. In the latter, an appropriate point that corresponds to the compressed shock surface ($\xi = 1_+$) must be found on the integrated curve. The physical quantities just behind the shock surface ($\xi = 1_-$) are then evaluated using the Ranking-Hugoniot relation, with which the numerical integration is continued along $\xi \to 0$. When the right point for $\xi = 1_+$ is found, the integration can be successfully terminated, such that eigenstructures for the density and velocity converge to the center, *i.e.*, $V_0 \to 0$, $G_0 \to 0$, and $Z_0 \to \infty$, as $\xi \to 0$.

Appendix B. – The perturbation quantities are postulated to be expanded in terms of spherical harmonics, $Y_\ell^m(\theta, \phi)$. A first-order variable is then introduced such as the total perturbation amplitude of the shock surface, given by $R(t)\,[1 + \Sigma(-t/\tau)^\sigma \eta_1^\ell Y_\ell^m]$ with normalized ℓ-th–mode amplitude η_1^ℓ; σ is the unknown growth rate, which is determined as an eigenvalue by solving the first-order system, derived by linearizing the fluid system, eqs. (1)–(3). Hereafter, we omit the summation Σ over the spherical harmonic modes for simplicity. Moreover we formulate the other variables such as the radial velocity $v = (r/t)[V_0(\xi) + (-t/\tau)^\sigma V_1(\xi) Y_\ell^m]$, the density $\rho = \rho_0[G_0(\xi) + (-t/\tau)^\sigma G_1(\xi) Y_\ell^m]$, and the squared speed of sound $c_s^2 = (r/t)^2[Z_0(\xi) + (-t/\tau)^\sigma Z_1(\xi) Y_\ell^m]$, where the last relation leads to $Z_1/Z_0 = P_1/P_0 - G_1/G_0$ with $Z_0 = \gamma P_0/G_0$. The transverse velocity $\mathbf{v}_\perp$ is not used in its explicit form, but instead, its divergence is used as a tractable form, *i.e.*, $r\nabla_\perp \cdot \mathbf{v}_\perp = (r/t)\,(-t/\tau)^\sigma\, D_1(\xi)\, Y_\ell^m$, where $\nabla_\perp$ denotes the transverse divergence operator with respect to the polar/azimuthal angles (θ, ϕ). Linearization of the perturbed fluid system gives the following ODEs:

$$\delta_1(G_0 V_1 + G_1 V_0) + \frac{\sigma G_1 + G_0 D_1}{\xi} - \alpha G_1' = 0, \qquad \text{(B.1)}$$

$$\Omega_0 V_1 + \xi\,(\Phi_0 V_1)' = \frac{G_1(\xi^2 P_0)' - G_0(\xi^2 P_1)'}{\xi G_0^2}, \qquad \text{(B.2)}$$

$$\Omega_0 D_1 + \xi \Phi_0 D_1' = \ell(\ell+1) P_1 G_0^{-1}, \qquad \text{(B.3)}$$

$$\delta_2 \left(\frac{P_1}{P_0} - \gamma \frac{G_1}{G_0} \right) + \frac{V_1}{\xi} \frac{\mathrm{d}\ln(\xi^2 P_0 G_0^{-\gamma})}{\mathrm{d}\ln\xi} = 0, \qquad \text{(B.4)}$$

where $\delta_1 = 3\xi^{-1} + (\mathrm{d}/\mathrm{d}\xi)$, $\delta_2 = \sigma\xi^{-1} + \Phi_0(\mathrm{d}/\mathrm{d}\xi)$, $\Omega_0 = 2V_0 + \sigma - 1$, and the prime denotes the derivative with respect to ξ. Equations (B.1)–(B.4) represent the conservation of mass, radial momentum, transverse momentum, and entropy, respectively. Deriving eq. (B.3), the relation, $r^2\nabla_\perp^2 Y_\ell^m = -\ell(\ell+1) Y_\ell^m$, has been used. The corresponding boundary conditions are also obtained from the conservation equations on the perturbed shock front:

$$V_1(1) = 2\,[\alpha(8\gamma+4) + (\gamma+1)(\sigma-3)]\,(\gamma+1)^{-2}, \qquad \text{(B.5)}$$

$$Z_1(1) = 4\gamma \left[\frac{5\gamma^2 - 6\gamma - 3}{\alpha^{-2}(\gamma+1)^3} + \frac{(\gamma-1)\sigma + 4 - 2\gamma}{\alpha^{-1}(\gamma+1)^2} \right], \qquad \text{(B.6)}$$

$$G_1(1) = 2\left[(5\gamma+1) - 3\alpha^{-1}(\gamma+1)\right](\gamma-1)^{-2}, \qquad \text{(B.7)}$$

$$D_1(1) = 2\ell(\ell+1)\alpha(\gamma+1)^{-1}, \qquad \text{(B.8)}$$

where all the above first-order perturbed quantities are given assuming $\eta = 1$.

The set of the perturbed system, eqs. (B.1)–(B.4), is numerically integrated under the boundary conditions, eqs. (B.5)–(B.8). The integration is terminated at the singular point, $\xi = \xi_0$, such that all the integrated curves for the perturbed quantities smoothly pass the singular point, as observed for the background quantities. Only an appropriate complex value of σ satisfies this condition as the eigenvalue. Note that a similar analysis to that given here can be found in ref. [15] with numerical values for $\ell \leqslant 8$.

REFERENCES

[1] Guderley G., *Luftfahrt-Forsch.*, **19** (1942) 302.
[2] Landau L. D. and Lifshitz E. M., *Fluid Mechanics* (Pergamon Press, Oxford) 1987.
[3] Stanukovich K. P., *Unsteady Motion of Continuous Media* (Pergamon Press, Oxford) 1960.
[4] Meyer-ter-Vhen J. and Schalk C., *Z. Naturforsch.*, **37a** (1982) 955.
[5] Perry R. *et al.*, *J. Appl. Phys.*, **22** (1951) 878.
[6] Takayama K. *et al.*, *Exp. Fluids*, **5** (1987) 315.
[7] Mdivnishvili M. *et al.*, *Shock Waves*, **9** (1999) 149.
[8] Atzeni S. and Meyer-ter-Vhen J., *The Physics of Inertial Fusion* (Clarendon Press, Oxford) 2004.
[9] Murakami M. and Nagatomo H., *Nucl. Instrum. Methods Phys. Res. A*, **544** (2005) 67.
[10] Azechi H. *et al.*, *Phys. Rev. Lett.*, **102** (2009) 235002.
[11] Betti R. *et al.*, *Phys. Rev. Lett.*, **98** (2007) 155001.
[12] Kidder R. E., *Nucl. Fusion*, **14** (1974) 53; 797.
[13] Barenblatt G. I., *Similarity, Self-Similarity, and Intermediate Asymptotics* (Consultants Bureau, New York) 1979.
[14] Gardner J., Book D. and Bernstein I., *J. Fluid. Mech.*, **114** (1982) 41.
[15] Brushlinskii K. V., *USSR Comput. Math. Math. Phys.*, **22** (1982) 193.
[16] Murakami M. *et al.*, *Phys. Plasmas*, **7** (2000) 2978.
[17] Zel'dovich Ya. B. and Raizer Yu. P., *Physics of Shock Waves and High Temperature Phenomena* (Academic Press, New York) 1966.
[18] Nuckolls J. *et al.*, *Nature*, **239** (1972) 193.
[19] Whitham G., *J. Fluid Mech.*, **2** (1957) 145.
[20] Chester W., *Philos. Mag.*, **45** (1954) 1293.
[21] Chisnell R. F., *Proc. R. Soc. London, Ser. A*, **232** (1955) 350.
[22] Henestroza E., Logan G. and Perkins J., *Phys. Plasmas*, **18** (2011) 032702; **19** (2012) 072706.